



PAPER • OPEN ACCESS

Radiation protection modelling for 2.5 Petawatt-laser production of ultrashort x-ray, proton and ion bunches: Monte Carlo model of the Munich CALA facility

To cite this article: Franz S Englbrecht *et al* 2020 *J. Radiol. Prot.* **40** 1048

View the [article online](#) for updates and enhancements.



BERTHOLD

Sensitive and flexible
detection of radioactive
contaminations

>Learn more

LB 940

Radiation protection modelling for 2.5 Petawatt-laser production of ultrashort x-ray, proton and ion bunches: Monte Carlo model of the Munich CALA facility

Franz S Englbrecht^{1,5} , Andreas Döpp², Jens Hartmann¹, Florian H Lindner¹ , Martin L Groß³, Hans-F Wirth³, Peter G Thirolf¹, Stefan Karsch², Jörg Schreiber^{1,4}, Katia Parodi¹ and George Dedes¹

¹ Department of Medical Physics, Faculty of Physics, Ludwig-Maximilians-Universität München, Am Coulombwall 1, 85748 Garching bei München, Germany

² Chair of Experimental Physics - Laser Physics, Faculty of Physics, Ludwig-Maximilians-Universität München, Am Coulombwall 1, 85748 Garching bei München, Germany

³ Laboratory for Extreme Photonics, Ludwig-Maximilians-Universität München, Am Coulombwall 1a, 85748 Garching bei München, Germany

⁴ Max Planck Institute of Quantum Optics, Hans-Kopfermann-Straße 1, 85748 Garching bei München, Germany

⁵ Author to whom any correspondence should be addressed.

E-mail: franz.englbrecht@physik.uni-muenchen.de

Received 12 May 2020; revised 17 July 2020

Accepted for publication 23 July 2020

Published 22 September 2020



CrossMark

Abstract

The ‘Centre for Advanced Laser Applications’ (CALA) is a new research institute for laser-based acceleration of electron beams for brilliant x-ray generation, laser-driven sub-nanosecond bunches of protons and heavy ions for biomedical applications like imaging and tumour therapy as well as for nuclear and high-field physics.

The radiation sources emerging from experiments using the up to 2.5 petawatt laser pulses with 25 femtosecond duration will be mixed particle-species of high intensity, high energy and pulsed, thus posing new challenges



Original Content from this work may be used under the terms of the [Creative Commons Attribution 4.0 licence](https://creativecommons.org/licenses/by/4.0/). Any further distribution of this work must maintain attribution to the author(s) and the title of the work, journal citation and DOI.

compared to conventional radiation protection. Such worldwide pioneering laser experiments result in source characteristics that require careful a-priori radiation safety simulations.

The FLUKA Monte-Carlo code was used to model the five CALA experimental caves, including the corridors, halls and air spaces surrounding the caves. Beams of electrons (< 5 GeV), protons (< 200 MeV), ^{12}C (< 400 MeV/u) and ^{197}Au (< 10 MeV/u) ions were simulated using spectra, divergences and bunch-charges based on expectations from recent scientific progress.

Simulated dose rates locally can exceed 1.5 kSv h^{-1} inside beam dumps. Vacuum pipes in the cave walls for laser transport and extraction channels for the generated x-rays result in small dose leakage to neighboring areas. Secondary neutrons contribute to most of the prompt dose rate outside caves into which the beam is delivered. This secondary radiation component causes non-negligible dose rates to occur behind walls to which large fluences of secondary particles are directed.

By employing adequate beam dumps matched to beam-divergence, magnets, passive shielding and laser pulse repetition limits, average dose rates in- and outside the experimental building stay below design specifications ($< 0.5 \mu\text{Sv h}^{-1}$) for unclassified areas, $< 2.5 \mu\text{Sv h}^{-1}$ for supervised areas, $< 7.5 \mu\text{Sv h}^{-1}$ maximum local dose rate) and regulatory limits ($< 1 \text{ mSv a}^{-1}$ for unclassified areas).

Keywords: radiation protection, monte carlo simulation, laser, ultrashort radiation bunches, accelerator, beam dump

(Some figures may appear in colour only in the online journal)

1. Introduction

Since the theoretical prediction of electron acceleration driven by high peak power femto-second lasers in 1979, the development of techniques to increase the peak power of lasers, led to the development of femtosecond (fs) short petawatt (PW) class lasers for particle acceleration [1, 2].

The ‘Centre for Advanced Laser Applications’ (CALA) in Garching, near Munich (Germany) is intended for laser-based acceleration of electron beams for brilliant x-ray generation (‘Laser-driven Undulator x-ray Source’ beamline (LUX), ‘Electron and Thomson Test Facility’ beamline (ETTF), ‘Source for Powerful Energetic Compact Thomson Radiation Experiments’ beamline (SPECTRE)) and laser-driven nanosecond bunches of protons and heavy ions (‘Laser-driven Ion Acceleration’ beamline (LION), ‘High Field’ beamline (HF)) for the investigation of the laser-acceleration and application of energetic protons and ions.

Laser-accelerated ion bunches have been proposed for use in radiation therapy of cancer [3]. Albeit the source characteristics of laser-accelerated ion bunches differ significantly from those of conventional sources, the former can be utilised in a wide range of novel biomedical applications and offer distinct advantages: reasonable compactness and cost effectiveness, synchronisation to laser pulses at a picosecond level, simple target and hence particle species changeability, broad energy spectrum, small source size, down to nanosecond bunch duration, allowing to use new bunch detection techniques and to study ultrashort biological effects [4–7].

Table 1. Laser systems installed in CALA and some of their main operation parameters.

	ATLAS-3000	PFS-pro
Power (10^{12} W)	2500	10
Pulse length (fs)	25	≤ 30
Pulse Energy (J)	60	0.1
Wavelength (nm)	750–850	700–1400
Shot frequency (Hz)	1	1000

Laser-accelerated electron beams can be used for various imaging applications (e.g. through the generation of x-ray and gamma ray secondary sources) and, at the same time, enable and validate innovative radiation generation mechanisms [8, 9].

The source characteristics can be changed through the choice of laser parameters and targets. Based on electron bunches accelerated in a plasma, these sources can be tailored to have the necessary properties of being compact and of delivering collimated, incoherent, and femto-second pulses of x-ray radiation [5, 10, 11].

The ionising radiation emerging from the experiments using the up to 2.5 PW laser pulses with 25 fs duration will be mixed particle species of high intensity, high maximum energy, broad energy spectrum and short duration; thus posing new challenges on shielding and monitoring compared to conventional radiation protection. The mixed particle species' nature of the bunches impedes the usage of conventional particle specific shielding concepts.

Conventional radiation protection mazes are designed such that particles need to undergo at least two scatters to escape the room. Such designs, which avoid straight penetrations as straight paths, can not be applied in CALA, since the optical laser pulses need to enter the experimental caves through straight penetration holes. Their diameter should be also large enough to keep the power density on the laser mirrors below their damage threshold.

As part of the legal regulations, areas in the CALA building have to be subdivided in the radiation protection categories unclassified, supervised and exclusion areas, based on the predominant prompt dose-rate to be expected [12]. Personal electronic dosimeters, as required in controlled radiation protection areas, have been reported to be unusable due to under-response already for bunches of ms duration [13–15].

Detailed dose rate estimations from Monte Carlo simulations can provide the insight necessary to categorise the local radiation exposure, especially since the envisioned particle source terms are still subject of active research and have not yet been reached experimentally.

We report here the results of Monte Carlo simulations of different source types relevant to various CALA experiments, in terms of calculated dose rates, with respect to established dose limits.

2. Materials and methods

2.1. CALA laser systems

The Centre for Advanced Laser Applications hosts two unique laser systems to drive the ionising radiation produced in laser-plasma experiments: ATLAS-3000 and PFS-pro.

2.1.1. ATLAS-3000 laser system. The workhorse of CALA is the 'Advanced Titanium-Sapphire Laser' system ATLAS-3000, which uses the chirped pulsed amplification (CPA) technique and has been operated for 20 years now and subsequently upgraded to reach a peak

power of up to 2.5 PW. Its main specifications are summarised in table 1. This peak power makes ATLAS the highest peak power laser system operated by a university in Europe in 2020. ATLAS is used to drive the experiments in LION, HF, ETTF, LUX and SPECTRE.

Its infrared pulses (central wavelength $\lambda = 800$ nm) contain an energy (after pulse compression) of up to 60 J in a duration of 25 fs and are guided as a 28 cm diameter beam via the evacuated laser beam delivery from the laser hall to five dedicated experimental rooms called caves. There, they are focused by off-axis parabolic mirrors down to micrometer small spot sizes.

By placing solid targets or gas jets in the focus, the intensity of up to 10^{23} W/cm² drives electrons or ions to relativistic velocities (see table 2). Those targets absorb the laser and represent the source of energetic particles, i.e. the source of the accelerator. The pulse repetition frequency on target can reach up to 1 Hz.

2.1.2. PFS-pro laser system. The Petawatt Field Synthesizer laser system (PFS-pro) is the second laser system under development in CALA with unique broadband laser characteristics (see table 1). Once completed, PFS-pro will seed the SPECTRE experiment.

Using a repetition frequency of up to 1 kHz, the SPECTRE experiment will use the highly energetic photons (50 keV – 200 keV) to generate x-rays by acceleration of electrons up to 70 MeV (see table 2). The x-rays will be used for medical imaging, among other applications.

2.2. CALA building and cave infrastructure

The five caves corresponding to the five CALA experiments are arranged around a central beam dump of 5.85 m thickness (figure 1). Due to the design of the CALA facility, the walls of the experimental caves, the roof and the floor as well as the central beam dump are the critical components that shield the exterior and the other experimental areas. Surrounding the five experimental caves are: a hall southeast of the central beam dump (labelled as 'Experimental hall' in figure 1) that will host x-ray cabins for x-ray experiments, on the south a laboratory area (labelled as 'Laboratory' in figure 1) and several corridors. The laser beam line (indicated by the dashed lines in figure 1) enters the five experimental caves through several penetration holes through the interior walls of CALA.

The central beam dump, walls, roof and cave doors consist of magnetite concrete (orange in figure 2) and magnetite aggregate of various water content (purple in figure 2) in a sandwich-like structure between either concrete or steel container walls. Such technically easy to realise sandwich-like construction was used for radiation protection buildings previously [22]. For CALA, the magnetite was compacted to a density of $\rho = 4.0$ t/m³ and allowed for thinner shielding walls at less cost. The used magnetite filling without cementitious interconnection is sustainable, since it can be reused after the operation of CALA will have ended, in contrast to regular heavy concrete [22]. The floor is made of 75 cm standard concrete using Portland cement to shield the groundwater from the radiation. The roof on top of the caves is 90 cm of compacted magnetite aggregate filled into rectangular steel pipes.

All caves (except of HF) are 18 m long, 3 m wide and 4.25 m high. The shorter HF cave is 13.81 m long, 4.3 m wide and 4.25 m high. A false floor is placed at 1 m above the concrete floor. The 20 cm radius laser penetration holes are located 50 cm below the false floor (see figure 3 for details of the modelled geometry at the beam line level). These holes are locations where dose can potentially leak outside of the experimental caves and are of particular interest in our study. Movable steel doors of 1 m thickness filled with magnetite aggregate seal the entrance to the caves during experiments.

Table 2. Simulated particle source parameters of the five experiments in CALA: LION and HF [4, 17–19] as well as LUX and ETTF [5, 10, 11] are seeded by ATLAS-3000. SPECTRE can be seeded by ATLAS and PFS-pro.

	Beam com- ponent	Energy spectrum [MeV]	Spectral shape	Full divergence angle [mrad]	Charge per pulse [nC]	Shot fre- quency [Hz]
LION	^{12}C	10 – 400 MeV/u	Box	180	0.016	1
	p^+	10 – 200	Box	180	0.16	1
	e^-	10 – 1000	e^-x	$10^3 / E[\text{MeV}]$	1.6	1
HF	^{197}Au	1 – 10 MeV/u	Box	200	0.016	1
	^{12}C	10 – 200 MeV/u	Box	200	0.016	1
	p^+	10 – 200	Box	200	0.16	1
LUX	e^-	10 – 1000	e^-x	$10^3 / E[\text{MeV}]$	1.6	1
	e^-	5000	Mono	2	1	1
	e^-	10 – 5000	Box	2	1	1
ETTF	e^-	5000	Mono	2	1	1
	e^-	10 – 5000	Box	2	1	1
SPECTRE	e^-	70	Mono	10	0.025	1000
	e^-	500	Mono	10	0.25	1
	e^-	10 – 500	Box	10	0.5	1

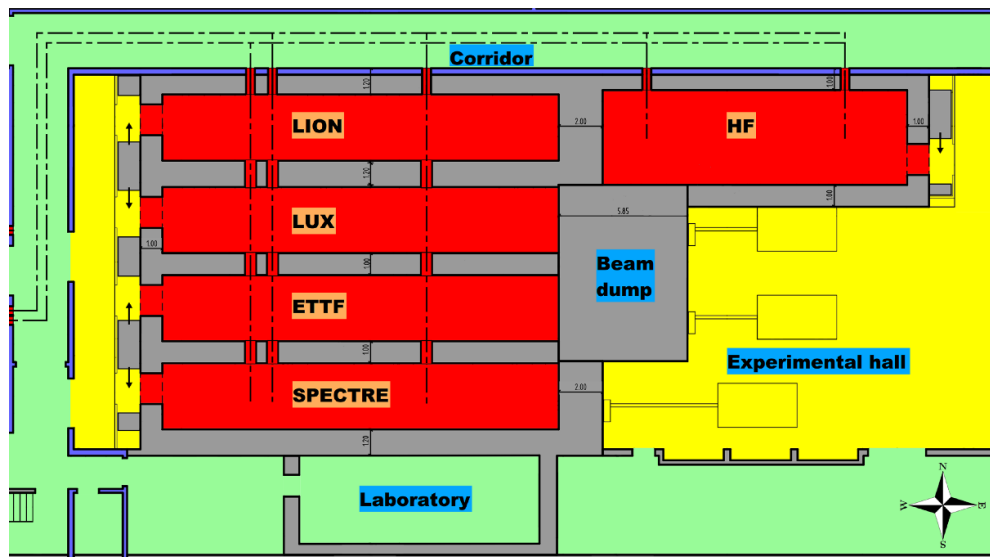


Figure 1. Structural and radiation zoning layout of the CALA facility. The five experimental caves are arranged around the central beam dump. East of the beam dump is an experimental hall hosting experiments inside x-ray cabins. Each active cave is an exclusion area (red), supervised areas are access limited (yellow). Areas like the transport corridor and a laboratory room are unclassified areas (green) based on the expected dose rate estimate. Sliding doors (moving in the direction of the arrows) can lock the active caves. Laser pulses can enter the caves through the transport beam line (dashed lines).

Due to the high power density of the laser pulses, the interaction between pulse and solid or gas target is performed in high vacuum (10^{-6} mbar). Above the false floor, the caves contain large vacuum chambers (depicted as white boxes in figure 2). The cubic modules ($1.21 \times 0.98 \times 1 \text{ m}^3$) are made of 2.5 cm thick aluminium plates mounted on steel frames and are connected to the beamline vacuum pipe system. Each chamber weighs 1.2 tons.

The details of the structures in each experimental cave relevant to this radiation protection investigation are described in the following.

2.3. CALA experiments

2.3.1. Laser-driven Ion Acceleration (LION). The LION experiment (see figure 1) places 10 nm – 1000 nm thin plastic, metal or diamond-like carbon foils targets into the focused ATLAS pulses. The targets are located 232 cm above the concrete floor. The high electric field of the laser pulse drives the electrons out of the foil. They form a sheath at the target rear boundary [23]. The arising field gradient between displaced electrons and foil nuclei can reach up to TeV/m and accelerates the hydrogen or carbon contamination on the foil surface up to hundreds of MeV (see table 2), which then propagate to the east towards the LION beam dump.

On its south side the LION cave borders with the LUX cave and on the east side with the HF beam line. On the north and west side it adjoins the north corridor and the entrance hall to the experimental areas, respectively.

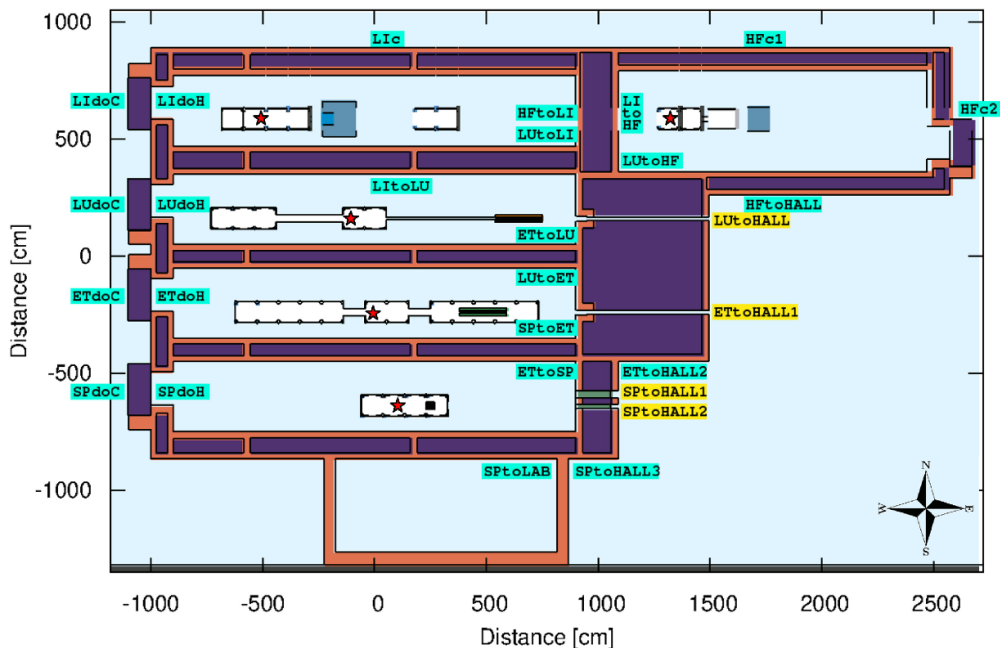


Figure 2. Layout of the CALA geometry model implemented in FLUKA. The 2D cross section was taken at the height in which the laser impinges onto the targets. These positions are indicated with a star in each cave and the beams are propagated in general eastwards. The vacuum chambers (in white) as well as the LION (gray -blue) and HF beam dumps (gray) are also shown. The labels indicate critical locations where the dose was quantified within cylindrical volumes. Turquoise and yellow colours correspond to two different radii of these cylindrical volumes.

Walls of 1.0 m – 1.2 m thickness are employed in order to keep the dose rates outside the cave below the designated levels. The wall in forward direction towards the east is 2 m thick and shields the HF cave during beam operation in LION. Three laser penetration holes (see figure 3) are running through the north (corridor - LION) and south walls (LION - LUX).

The cave geometry model (see figure 2) contains a set of four vacuum chambers for the acceleration experiment and two for offline tests without ATLAS.

A dedicated, hybrid beam dump (see figure 2) was designed for LION with the purpose of stopping the beam and containing as much as possible of the primary and secondary particles' fluence and dose. The size of the beam dump is 1.5 m × 1.5 m × 1.5 m. It is made of heavy concrete, except for a cubic volume of 0.5 m × 0.5 m × 0.5 m filled with water. The water tank is placed in the middle of the beam dump on the vertical and horizontal dimension and starts at the front face of the beam dump.

2.3.2. High-Field (HF). The HF experiment aims to explore the acceleration and interaction characteristics of ultrashort and intense ion bunches [20]. Electrons, protons and heavier ions will be accelerated using foil targets (see table 2). The goal is preparatory research for the generation of extremely neutron-rich isotopes to answer questions in astrophysical nucleosynthesis of heavy elements like gold and uranium by experimentally realising the fission-fusion reaction mechanism, which is yet inaccessible using conventional particle accelerators [21].

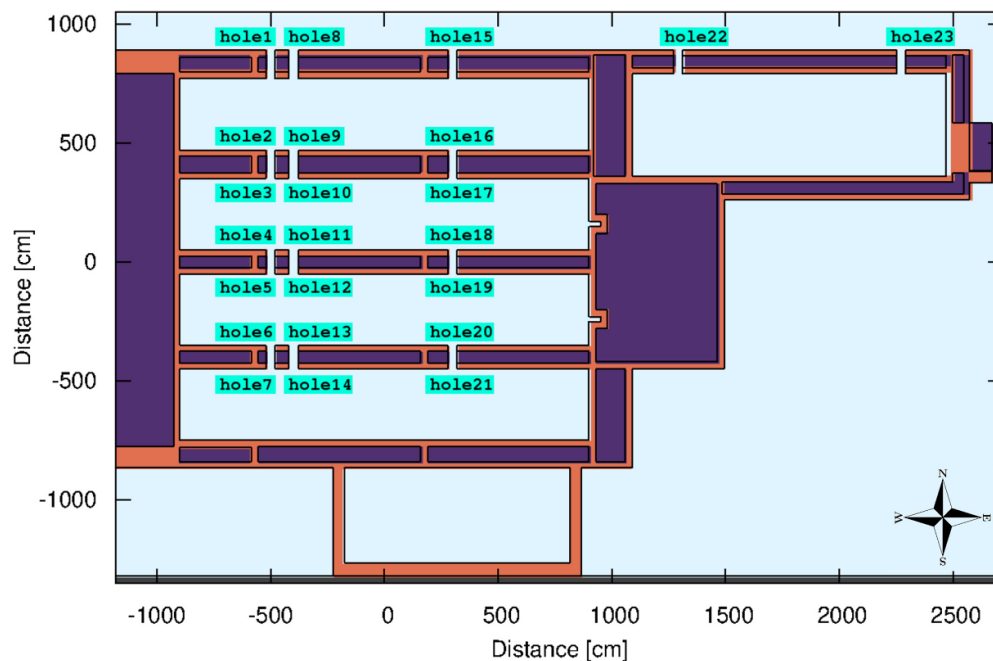


Figure 3. Layout of the CALA geometry model implemented in FLUKA. The 2D cross section was taken at the height in which the laser enters the caves. The labels indicate critical locations where the dose was quantified within cylindrical volumes.

On its south side, the HF cave borders with the experimental hall for x-ray experiments outside the ETTF and LUX cave and the central beam dump. On the west side the LION cave is behind the 2 m thick wall. On the north and east side it adjoins the north corridor and the entrance hall to the experimental areas, respectively.

Two vacuum chambers (see figure 2) are connected by a 25 cm long pipe ($r = 15.9$ cm) to a special chamber for the HF experiment ($0.85 \times 0.8 \times 1.25 \text{ m}^3$).

Since the primary radiation from the laser-driven source in HF is similar to LION - protons and heavier ions, the HF beam dump is similar. The heavy concrete beam dump is $1 \text{ m} \times 1 \text{ m} \times 1 \text{ m}$ and stops the ion bunches and secondary particles, which are emitted 227 cm above the concrete floor. The beam dump geometry model is shown in figure 2.

The outer walls of HF are 1 m thick. Two laser penetration holes (see figure 3) are running through the north (corridor - HF) wall.

2.3.3. Laser-driven Undulator X-ray source (LUX). The LUX experiment is set for generating brilliant x-ray undulator radiation using a magnetic undulator seeded by up to 5 GeV laser accelerated electrons. In full operation, it may serve as a prototype laser-plasma-accelerator based free-electron laser (FEL) for biomedical x-ray imaging experiments.

On its north side, LUX is separated from LION by a 1.2 m wall. On its south side it borders the ETTF cave via a 1 m wall and the east side of the cave terminates with the central 5.85 m thick central beam dump. Three laser penetration holes are running through the north and three through the south walls (see figure 3).

Two vacuum chambers for laser preparation are connected by a 3 m long pipe ($r = 35$ cm) to three chambers for the interaction of pulse and gas target (220 cm above the concrete floor and propagating to the east). A 2.1 m long permanent magnet ($B = 0.85$ T) follows 4.87 m after the chamber. The magnet serves as diagnostic element for the electron spectrum and as a radiation protection device by bending the electrons downwards into the 5.85 m central beam dump.

Only the generated x-rays pass the magnet travelling straight and may traverse the central beam dump through a cylindrical 7.5 cm radius channel which is on axis with the laser propagation. All the above elements have been implemented in the LUX cave geometry model (see figure 2).

2.3.4. Electron and Thomson Test Facility (ETTF). The ETTF experiment is a fundamental research experiment to generate brilliant hard x-rays via Thomson-backscattering and betatron radiation from ATLAS-3000 pulses. Up to 5 GeV laser-accelerated electrons (see table 2) and their characteristics like charge, space charge, timing and acceleration mechanism are probed experimentally, in order to provide x-rays best suited for biomedical experiments like phase contrast imaging or ultrafast phenomena in solids and matter in the plasma state [8, 9].

On its north side, ETTF borders with LION and south with SPECTRE, both separated from ETTF by a 1 m thick wall. Like LUX, the east end of the cave is the 5.85 m central beam dump with a $r = 7.5$ cm radius cylindrical channel for x-rays. Three laser penetration holes have the same dimensions as for LUX and are running through the north and through the south walls (see figure 3).

Three sets of chambers (five, two and five chambers in each set) connected by pipes were implemented into the geometry model (see figure 2). The interaction point of the laser pulse and the target is located 220 cm above the concrete floor and the beam propagates eastwards. The last set of chambers hosts the same 2.1 m permanent magnet ($B = 0.85$ T) as in LUX. The magnet again is used for electron energy diagnostic and as a radiation protection device by bending the electrons downwards.

For one special experiment only, the magnet will be removed, causing the 5 GeV beam to be directly aiming at the x-ray penetration hole in the 5.85 m central beam dump. In order to keep the experimental hall dose within the legal dose rate limits, the channel will be shielded using lead bricks before and after the channel.

2.3.5. Source for powerful energetic compact thomson radiation experiments (SPECTRE). The SPECTRE experiment uses both ATLAS (up to 300 TW) and PFS-pro as driving laser. Using ATLAS, SPECTRE aims to accelerate electron bunches of 0.25 nC – 0.5 nC up to 500 MeV for x-ray generation. At the PFS-pro repetition rate of up to 1 kHz, a tunable source of x-rays for biomedical experiments using up to 70 MeV electron beams will be established. Further source characteristics are listed in table 2.

On its north side, SPECTRE borders with ETTF and on the south with a laboratory, both separated from SPECTRE by 1 m thick walls. The north wall has three laser penetration holes (see figure 3). The east wall of 1.9 m thickness shields the experimental hall from radiation created in SPECTRE and has two cylindrical holes to allow for the extraction of the x-rays. For most experiments, the two holes will be plugged with S235JR steel bars.

A set of four chambers is installed and uses a 40 cm permanent magnet ($B = 0.85$ T) for energy diagnostic and radiation protection. The chambers and the magnet are included in the SPECTRE geometry model as shown in figure 2.

The particle bunches will be emitted 219.5 cm above the concrete floor and propagate eastwards.

2.4. Monte Carlo simulations

All radiation protection calculations presented in this study were performed with the FLUKA Monte-Carlo code version FLUKA2011.2x.2. FLUKA is a general purpose tool for calculations of particle transport and interactions with matter, covering an extended range of applications [24, 25]. It can simulate with high accuracy the interaction and propagation in matter of about 60 different particles, with energies ranging from the keV to the TeV scale.

The PRECISIO physics settings were chosen for all simulations. Neutrons were transported down to thermal energies, electrons down to 1.5 MeV, photons to 1 keV and all other particles down to 100 keV. Option EMF was used to request a detailed transport of electrons, positrons and photons.

A detailed geometry model of the five experimental caves and surrounding structures was implemented. The geometry model included the walls, doors, roof, vacuum chambers, spectrometer magnets and beam dumps, all characterised by their dimensions, elemental composition, mass density and for the magnet, field strength. The vacuum pipes for the laser and other chamber content have not been included in the model.

Two horizontal cross sections of the detailed geometry model are shown: one at the height where the laser pulses impinged on the target (figure 2) and one at the height where the laser enters the experimental caves (figure 3).

As sources, electrons (< 5 GeV), protons (< 200 MeV), ^{12}C -ions (< 400 MeV/u) and ^{197}Au -ions (< 10 MeV/u) were simulated using spectra, divergences and bunch-charges based on expectations from recent experimental results [10, 27]. Source characteristics are summarised in table 2. The assumed particle energies and bunch charges were optimistic upper boundaries, that account for the most challenging scenarios in terms of radiation protection.

The bunch divergences expected experimentally for proton or laser ion acceleration experiments (LION, HF) are, almost entirely, covered by the in-cave beam dumps and have hence been modelled using the scaling law in table 2 or worst case values. There are ions also emitted at larger angles, but due to their low energy fluence they would not be relevant for radiation protection. For laser-driven electron acceleration the generated particle beam is very directional, with a divergence of typically one mrad [26]. The angular pointing jitter is of a similar order and thus approximated using a fixed value (table 2).

For LION and HF, the simulated sources were mixed radiation fields (ions plus electrons). To simplify the simulations while allowing for detailed interpretation of the results, each initial component of a mixed radiation field was simulated separately and summed up in post processing to yield the total equivalent dose.

For the dosimetric evaluation of the results, the equivalent dose in units of pSv/primary particle was scored in a three dimensional Cartesian mesh (USRBIN scorer) with a voxel size of $10\text{ cm} \times 10\text{ cm} \times 10\text{ cm}$. To allow for a detailed investigation of different contributions, the total equivalent dose was decomposed to dose from neutrons, photons and, when deemed necessary, from electrons.

At critical locations, where elevated doses were expected, the dose equivalent was also scored in cylindrical air volumes of various radii and 5 cm thickness. The locations of these cylindrical scorers is indicated in figure 2, and figure 3, bearing the scorer's name. In turquoise are indicated scorers with 50 cm radius and in yellow with radii of 15 cm to 32.4 cm, depending on the size of the hole preceding them.

The radiation dose limits (see next section 2.5 for more details) are expressed in units of micro-Sievert per hour ($\mu\text{Sv h}^{-1}$). The scored dose in pSv/primary needed therefore to be converted to $\mu\text{Sv h}^{-1}$ via a conversion factor. The conversion factor c was generally different for each simulation and source component and was calculated as follows:

$$c = N \cdot R \cdot U. \quad (1)$$

where N is the number of particles produced per laser shot, R the number of laser shots per hour (repetition rate) and $U = 10^{-6}$ is a dimensionless conversion factor from pSv to μSv .

2.5. Radiation limits

The CALA facility, in terms of radiation protection, can be regarded in three categories: exclusion, supervised and unclassified areas. The upper radiation dose rate limits were defined in agreement with the Bavarian Environment Agency (Bayerisches Landesamt für Umwelt).

In the CALA plan showed in figure 1, the north and west corridors and the southern laboratory are the only unclassified areas. The radiation dose rate limit in an unclassified area is $0.5 \mu\text{Sv h}^{-1}$ in order to ensure an accumulated dose of less than 1 mSv per year, assuming a 2000h annual occupancy. A local maximum of about $2 \mu\text{Sv h}^{-1}$ is tolerable if monitored and/or not accessible.

All experimental caves, the air space above them and the experimental hall were categorised as supervised areas. The CALA design goal for supervised areas was $2.5 \mu\text{Sv h}^{-1}$ with a local maximum allowed to reach $7.5 \mu\text{Sv h}^{-1}$. These locations will then be made inaccessible or marked with a warning sign.

When the laser is in full operation in a cave, then that particular cave is closed and classified as an exclusion area, while the other caves remain supervised areas. There is no upper dose rate limit specified in exclusion areas, as long as the dose rate limits in surrounding supervised or unclassified areas are not violated.

During the present trial operation of the CALA facility, continuous dose measurements are performed with passive thermoluminescent dosimeters (TLDs) on up to ten locations and evaluated monthly. Their values have to be reported quarterly to the Bavarian Environment Agency.

Thus, controlled areas with the duty to wear personal electronic dosimeters can be avoided. This might change in future operation because of activations and the resulting dose rate they might cause. However, this has not been observed yet in CALA but would cause no basic problems since the radiation would not be pulsed and dosimeters are available.

3. Results

Our simulations showed that, due to the high particle fluence ($\approx 10^{10}$ particles/cm²) in a cave during operation, the dose rate can exceed 1.5 kSv/h. The peak dose rate occurred, for each cave, in the respective beam dump, but dose rates higher than $10 \mu\text{Sv h}^{-1}$ were present in large sections of each cave during operation of the laser (e.g. figure 4).

Depending on the cave and the beam dump geometry and location, different critical points were identified as indicated in figure 2 and figure 3. These critical points were in general located either behind open holes (vacuum pipes) or behind walls, but in positions where large fluences of particles were directed. The dose escaping a cave, during operation in that particular cave, and quantified at these critical locations, were summarised in tables 3–7. Dose rates above the dose rate limit are highlighted as bold numbers in the tables. For the experiments producing

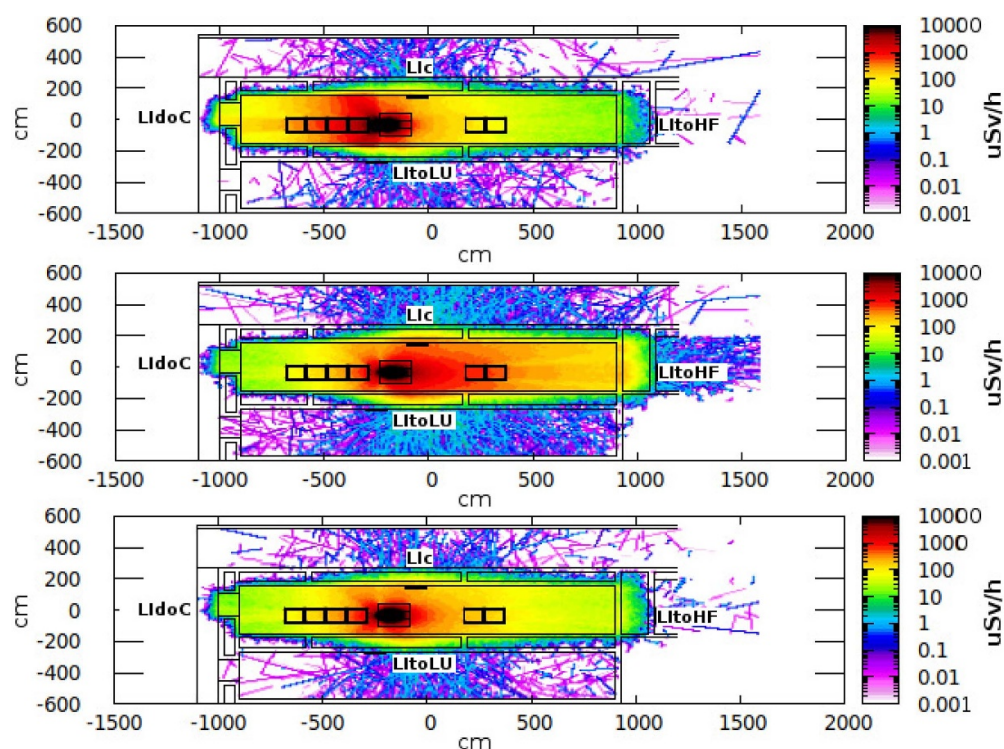


Figure 4. Dose rate distributions in and around the LION cave, plotted at the source height for different versions of the LION beam dump and for the ^{12}C ion beam component. (*top*) a version of the beam dump made entirely of concrete, (*middle*) the same beam dump volume filled with water and (*bottom*) the optimised beam dump, combining both water and concrete volumes. Some of the scoring locations relevant to LION are also indicated.

protons and heavier ions (LION and HF), the dose rate is listed as an electron beam component (same for all sources) and the respective proton or heavy ion beam component.

All estimated dose rates listed in tables 3–7 entail statistical uncertainties. These uncertainties were strongly dependent on the absolute dose rate and on the particle fluence in the location under consideration. For calculated dose rates larger than $1\ \mu\text{Sv h}^{-1}$, the statistical uncertainty ranged from 1% to 9%, with the mean error being 6%. For calculated dose rates between $0.1\ \mu\text{Sv h}^{-1}$ and $1\ \mu\text{Sv h}^{-1}$ the error ranged from 1% to 40%, with the mean error being 15% and errors above 20% associated uniquely to dose rates below $0.5\ \mu\text{Sv h}^{-1}$.

3.1. LION

As summarised in table 3, two source types were simulated for the LION cave: ^{12}C ions and protons. The same electron beam component was assumed for each of the two source types. For each beam component, the major contributions to dose rates (by neutrons and photons) alongside with the total dose rate are listed. Finally, the overall total dose rate for a given source type is shown in the right most column.

Table 3. Dose rate calculations for LION, at critical locations indicated in figure 2 and figure 3. The upper half of the table lists results for the ^{12}C source, while the lower half presents the same for the proton source.

Dose rate limit		Dose rate [$\mu\text{Sv h}^{-1}$]							
	Detector	Electron beam component			Carbon beam component				
		n	γ	Total	n	γ	Total		
LLION Carbon	0.5	Llc	6.86×10^{-2}	1.07×10^{-3}	7.11×10^{-2}	9.62×10^{-1}	1.55×10^{-2}	9.90×10^{-1}	1.06
	0.5	hole1	1.76×10^{-2}	1.29×10^{-2}	3.25×10^{-2}	1.95×10^{-1}	9.10×10^{-3}	2.07×10^{-1}	2.40×10^{-1}
	0.5	hole8	8.01×10^{-2}	1.45×10^{-3}	8.21×10^{-2}	2.73×10^{-1}	4.10×10^{-3}	2.81×10^{-1}	3.63×10^{-1}
	0.5	hole15	1.63×10^{-3}	2.89×10^{-3}	4.53×10^{-3}	4.75×10^{-1}	8.22×10^{-3}	4.92×10^{-1}	4.97×10^{-1}
	2.5	LltoHF	6.39×10^{-4}	1.14×10^{-5}	6.55×10^{-4}	2.04×10^{-1}	2.60×10^{-3}	2.13×10^{-1}	2.13×10^{-1}
	2.5	LltoLU	8.54×10^{-2}	1.28×10^{-3}	8.82×10^{-2}	1.61	2.70×10^{-2}	1.65	1.73
	2.5	Llroof	2.10×10^{-1}	1.72×10^{-3}	2.13×10^{-1}	3.03	3.79×10^{-2}	3.10	3.31
	2.5	LldoC	1.22×10^{-2}	1.38×10^{-4}	1.24×10^{-2}	6.37×10^{-3}	2.90×10^{-4}	6.66×10^{-3}	1.94×10^{-2}
	2.5	hole3	3.54×10^{-2}	2.74×10^{-2}	6.29×10^{-2}	2.32×10^{-1}	1.07×10^{-2}	2.44×10^{-1}	3.07×10^{-1}
	2.5	hole10	9.44×10^{-2}	5.85×10^{-3}	1.26×10^{-1}	2.87×10^{-1}	4.20×10^{-3}	4.00×10^{-1}	5.26×10^{-1}
2.5	hole17	6.47×10^{-3}	1.87×10^{-4}	6.68×10^{-3}	4.96×10^{-3}	7.35×10^{-3}	5.08×10^{-1}	5.15×10^{-1}	
LLION Proton	0.5	Llc	6.86×10^{-2}	1.07×10^{-3}	7.11×10^{-2}	1.75×10^{-2}	3.79×10^{-4}	1.80×10^{-2}	8.91×10^{-2}
	0.5	hole1	1.76×10^{-2}	1.29×10^{-2}	3.25×10^{-2}	7.43×10^{-2}	3.22×10^{-3}	7.94×10^{-2}	1.12×10^{-1}
	0.5	hole8	8.01×10^{-2}	1.45×10^{-3}	8.21×10^{-2}	2.72×10^{-2}	7.29×10^{-4}	2.85×10^{-2}	1.12×10^{-1}
	0.5	hole15	1.63×10^{-3}	2.89×10^{-3}	4.53×10^{-3}	1.13×10^{-2}	3.07×10^{-4}	1.17×10^{-2}	1.62×10^{-2}
	2.5	LltoHF	6.39×10^{-4}	1.14×10^{-5}	6.55×10^{-4}	6.25×10^{-4}	7.71×10^{-6}	6.41×10^{-4}	1.30×10^{-3}
	2.5	LltoLU	8.54×10^{-2}	1.28×10^{-3}	8.82×10^{-2}	4.46×10^{-2}	7.32×10^{-4}	4.55×10^{-2}	1.34×10^{-1}
	2.5	Llroof	2.10×10^{-1}	1.72×10^{-3}	2.13×10^{-1}	8.52×10^{-2}	1.34×10^{-3}	8.72×10^{-2}	3.00×10^{-1}
	2.5	LldoC	1.22×10^{-2}	1.38×10^{-4}	1.24×10^{-2}	6.34×10^{-4}	2.85×10^{-5}	6.62×10^{-4}	1.30×10^{-2}
	2.5	hole3	3.54×10^{-2}	2.74×10^{-2}	6.29×10^{-2}	6.82×10^{-2}	2.44×10^{-3}	7.39×10^{-2}	1.37×10^{-1}
	2.5	hole10	9.44×10^{-2}	5.85×10^{-3}	1.26×10^{-1}	1.09×10^{-1}	3.73×10^{-3}	1.14×10^{-1}	2.40×10^{-1}
2.5	hole17	6.47×10^{-3}	1.87×10^{-4}	6.68×10^{-3}	5.28×10^{-3}	5.71×10^{-4}	6.13×10^{-3}	1.28×10^{-2}	

In the vast majority of critical locations the dose from neutrons was at least one order of magnitude higher than that from photons, which was the next highest contribution. Dose imparted to these critical points by other particles was negligible.

For the proton source, the total dose rate at all critical locations was below the $0.5 \mu\text{Sv h}^{-1}$ and $2.5 \mu\text{Sv h}^{-1}$ limit, for unclassified and supervised areas, respectively. For the ^{12}C ion source, the dose rate exceeded the limits in two locations: opposite to the beam dump on the corridor (LIc) the dose rate was estimated to be $1.06 \mu\text{Sv h}^{-1}$ ($0.5 \mu\text{Sv h}^{-1}$ limit) and on one location on the roof of the cave it was calculated to be $3.31 \mu\text{Sv h}^{-1}$ ($2.5 \mu\text{Sv h}^{-1}$ limit).

The results in table 3 were obtained with the hybrid (water - concrete) beam dump geometry, which helped to reduce the dose in the north corridor and through the laser penetration holes. Exemplary results are shown in figure 4, comparing a full concrete beam dump (figure 4 - top), a full water beam dump of the same volume (figure 4 - middle) and the hybrid beam dump of the same volume (figure 4 - bottom).

3.2. HF

Table 4 lists the dose rate calculations for HF, at the critical points shown in figure 2 and figure 3. Three source types were simulated for the HF cave: protons, ^{12}C ions and ^{197}Au ions. The same electron beam component was assumed for each of the three source types. For each beam component, the major contributions to dose rates from neutrons and photons and the total dose rate are listed.

The proton source calculations showed that the dose rate limit of $0.5 \mu\text{Sv/h}$ was mildly exceeded in two locations, at the corridor outside the HF cave (0.80 and $0.52 \mu\text{Sv/h}$, respectively). Behind one of the laser penetration holes leading to the north corridor (hole22), the dose rate was estimated to be $1.26 \mu\text{Sv h}^{-1}$, substantially higher than the $0.5 \mu\text{Sv h}^{-1}$, but well below $2.5 \mu\text{Sv h}^{-1}$. In the same locations the dose rate for the ^{12}C source was found to be 0.77 , 0.74 and $0.52 \mu\text{Sv h}^{-1}$. The dose rate outside of the HF cave for the ^{197}Au source has been calculated to be always below $0.5 \mu\text{Sv}$. In all cases the dose rate due to neutrons was at least an order of magnitude higher than due to photons.

3.3. LUX

The simulation results in table 5 summarise the dose rates at various positions outside the LUX cave for the two different electron spectra listed in table 2.

Since the primary source consists of highly penetrating electrons, the total dose rate is reported alongside with the individual contributions from neutrons, gammas and electrons.

For most scoring positions and for both the monoenergetic and the broad energy spectrum, the neutron dose rate was found to be the highest contribution to the total dose rate. The calculated dose rates from the broad spectrum electron source were mostly lower than the corresponding ones from the monoenergetic 5 GeV electron beam and always lower than the $2.5 \mu\text{Sv h}^{-1}$ design limit.

For the 5 GeV monoenergetic electron source, at all positions, except for the critical location behind the channel of the central beam dump (LUtoHALL), the dose rate was kept below the $2.5 \mu\text{Sv h}^{-1}$ design limit. At that particular location, the dose rate calculated was $6.95 \mu\text{Sv h}^{-1}$, which is still below the $7.5 \mu\text{Sv h}^{-1}$ maximum local dose rate limit.

3.4. ETTF

The simulation results in table 6 summarise the dose rates at various positions outside the ETTF cave for three experiments: the broad spectrum electron source with the spectrometer

Table 4. Dose rate calculations for HF, at critical locations indicated in figure 2 and figure 3. The *upper third* of the table lists results for the proton source, the *middle third* for the ^{12}C source, while the *lower third* holds for the ^{197}Au source.

Dose rate		Dose rate [$\mu\text{Sv h}^{-1}$]							
limit	Detector	Electron beam component			Proton beam component				
$[\mu\text{Sv}/h]$	position	n	γ	Total	n	γ	Total		
HF Proton	0.5	hole22	2.83×10^{-1}	1.65×10^{-2}	3.07×10^{-1}	9.01×10^{-1}	1.32×10^{-2}	9.56×10^{-1}	1.26
	0.5	hole23	2.70×10^{-2}	5.83×10^{-3}	3.34×10^{-2}	1.16×10^{-1}	4.86×10^{-3}	1.22×10^{-1}	1.55×10^{-1}
	0.5	HFcl	1.70×10^{-1}	3.21×10^{-3}	1.76×10^{-1}	6.12×10^{-1}	1.10×10^{-2}	6.27×10^{-1}	8.03×10^{-1}
	0.5	HFce	4.11×10^{-1}	7.37×10^{-3}	4.26×10^{-1}	9.57×10^{-2}	1.06×10^{-3}	9.69×10^{-2}	5.23×10^{-1}
	0.5	HFtoHALL	8.22×10^{-2}	1.52×10^{-3}	8.58×10^{-2}	2.65×10^{-1}	5.76×10^{-3}	2.73×10^{-1}	3.59×10^{-1}
	0.5	HFtoLI	$\mathcal{O}(10^{-5})$	$\mathcal{O}(10^{-6})$	$\mathcal{O}(10^{-5})$	0.00	1.14×10^{-8}	1.30×10^{-8}	1.30×10^{-8}
	2.5	HFroof	2.95×10^{-1}	4.87×10^{-3}	3.54×10^{-1}	4.49×10^{-1}	4.84×10^{-3}	4.56×10^{-1}	8.10×10^{-1}
HF Carbon	0.5	hole22	2.83×10^{-1}	1.65×10^{-2}	3.07×10^{-1}	2.02×10^{-1}	6.05×10^{-3}	2.10×10^{-1}	5.17×10^{-1}
	0.5	hole23	2.70×10^{-2}	5.83×10^{-3}	3.34×10^{-2}	1.49×10^{-1}	3.67×10^{-3}	1.56×10^{-1}	1.89×10^{-1}
	0.5	HFcl	1.70×10^{-1}	3.21×10^{-3}	1.76×10^{-1}	5.70×10^{-1}	1.09×10^{-2}	5.91×10^{-1}	7.66×10^{-1}
	0.5	HFce	4.11×10^{-1}	7.37×10^{-3}	4.26×10^{-1}	2.98×10^{-1}	6.57×10^{-3}	3.15×10^{-1}	7.41×10^{-1}
	0.5	HFtoHALL	8.22×10^{-2}	1.52×10^{-3}	8.58×10^{-2}	3.65×10^{-1}	7.14×10^{-3}	3.83×10^{-1}	4.69×10^{-1}
	0.5	HFtoLI	$\mathcal{O}(10^{-5})$	$\mathcal{O}(10^{-6})$	$\mathcal{O}(10^{-5})$	1.34×10^{-5}	2.09×10^{-7}	1.36×10^{-5}	1.36×10^{-5}
	2.5	HFroof	2.95×10^{-1}	4.87×10^{-3}	3.54×10^{-1}	4.97×10^{-1}	5.05×10^{-3}	5.05×10^{-1}	8.59×10^{-1}
HF Gold				Electron beam component			Carbon beam component		
	0.5	hole22	2.83×10^{-1}	1.65×10^{-2}	3.07×10^{-1}				
	0.5	hole23	2.70×10^{-2}	5.83×10^{-3}	3.34×10^{-2}				
	0.5	HFcl	1.70×10^{-1}	3.21×10^{-3}	1.76×10^{-1}				
	0.5	HFce	4.11×10^{-1}	7.37×10^{-3}	4.26×10^{-1}				
	0.5	HFtoHALL	8.22×10^{-2}	1.52×10^{-3}	8.58×10^{-2}				
	0.5	HFtoLI	$\mathcal{O}(10^{-5})$	$\mathcal{O}(10^{-6})$	$\mathcal{O}(10^{-5})$				
HF Gold				Electron beam component			Gold beam component		
	0.5	hole22	2.83×10^{-1}	1.65×10^{-2}	3.07×10^{-1}				
	0.5	hole23	2.70×10^{-2}	5.83×10^{-3}	3.34×10^{-2}				
	0.5	HFcl	1.70×10^{-1}	3.21×10^{-3}	1.76×10^{-1}				
	0.5	HFce	4.11×10^{-1}	7.37×10^{-3}	4.26×10^{-1}				
	0.5	HFtoHALL	8.22×10^{-2}	1.52×10^{-3}	8.58×10^{-2}				
	0.5	HFtoLI	$\mathcal{O}(10^{-5})$	$\mathcal{O}(10^{-6})$	$\mathcal{O}(10^{-5})$				
2.5	HFroof	2.95×10^{-1}	4.87×10^{-3}	3.54×10^{-1}					
HF Gold	0.5	hole22	2.83×10^{-1}	1.65×10^{-2}	3.07×10^{-1}				
	0.5	hole23	2.70×10^{-2}	5.83×10^{-3}	3.34×10^{-2}				
	0.5	HFcl	1.70×10^{-1}	3.21×10^{-3}	1.76×10^{-1}				
	0.5	HFce	4.11×10^{-1}	7.37×10^{-3}	4.26×10^{-1}				
	0.5	HFtoHALL	8.22×10^{-2}	1.52×10^{-3}	8.58×10^{-2}				
	0.5	HFtoLI	$\mathcal{O}(10^{-5})$	$\mathcal{O}(10^{-6})$	$\mathcal{O}(10^{-5})$				
	2.5	HFroof	2.95×10^{-1}	4.87×10^{-3}	3.54×10^{-1}				
HF Gold	0.5	hole22	2.83×10^{-1}	1.65×10^{-2}	3.07×10^{-1}				
	0.5	hole23	2.70×10^{-2}	5.83×10^{-3}	3.34×10^{-2}				
	0.5	HFcl	1.70×10^{-1}	3.21×10^{-3}	1.76×10^{-1}				
	0.5	HFce	4.11×10^{-1}	7.37×10^{-3}	4.26×10^{-1}				
	0.5	HFtoHALL	8.22×10^{-2}	1.52×10^{-3}	8.58×10^{-2}				
	0.5	HFtoLI	$\mathcal{O}(10^{-5})$	$\mathcal{O}(10^{-6})$	$\mathcal{O}(10^{-5})$				
	2.5	HFroof	2.95×10^{-1}	4.87×10^{-3}	3.54×10^{-1}				
HF Gold	0.5	hole22	2.83×10^{-1}	1.65×10^{-2}	3.07×10^{-1}				
	0.5	hole23	2.70×10^{-2}	5.83×10^{-3}	3.34×10^{-2}				
	0.5	HFcl	1.70×10^{-1}	3.21×10^{-3}	1.76×10^{-1}				
	0.5	HFce	4.11×10^{-1}	7.37×10^{-3}	4.26×10^{-1}				
	0.5	HFtoHALL	8.22×10^{-2}	1.52×10^{-3}	8.58×10^{-2}				
	0.5	HFtoLI	$\mathcal{O}(10^{-5})$	$\mathcal{O}(10^{-6})$	$\mathcal{O}(10^{-5})$				
	2.5	HFroof	2.95×10^{-1}	4.87×10^{-3}	3.54×10^{-1}				
HF Gold	0.5	hole22	2.83×10^{-1}	1.65×10^{-2}	3.07×10^{-1}				
	0.5	hole23	2.70×10^{-2}	5.83×10^{-3}	3.34×10^{-2}				
	0.5	HFcl	1.70×10^{-1}	3.21×10^{-3}	1.76×10^{-1}				
	0.5	HFce	4.11×10^{-1}	7.37×10^{-3}	4.26×10^{-1}				
	0.5	HFtoHALL	8.22×10^{-2}	1.52×10^{-3}	8.58×10^{-2}				
	0.5	HFtoLI	$\mathcal{O}(10^{-5})$	$\mathcal{O}(10^{-6})$	$\mathcal{O}(10^{-5})$				
	2.5	HFroof	2.95×10^{-1}	4.87×10^{-3}	3.54×10^{-1}				
HF Gold	0.5	hole22	2.83×10^{-1}	1.65×10^{-2}	3.07×10^{-1}				
	0.5	hole23	2.70×10^{-2}	5.83×10^{-3}	3.34×10^{-2}				
	0.5	HFcl	1.70×10^{-1}	3.21×10^{-3}	1.76×10^{-1}				
	0.5	HFce	4.11×10^{-1}	7.37×10^{-3}	4.26×10^{-1}				
	0.5	HFtoHALL	8.22×10^{-2}	1.52×10^{-3}	8.58×10^{-2}				
	0.5	HFtoLI	$\mathcal{O}(10^{-5})$	$\mathcal{O}(10^{-6})$	$\mathcal{O}(10^{-5})$				
	2.5	HFroof	2.95×10^{-1}	4.87×10^{-3}	3.54×10^{-1}				
HF Gold	0.5	hole22	2.83×10^{-1}	1.65×10^{-2}	3.07×10^{-1}				
	0.5	hole23	2.70×10^{-2}	5.83×10^{-3}	3.34×10^{-2}				
	0.5	HFcl	1.70×10^{-1}	3.21×10^{-3}	1.76×10^{-1}				
	0.5	HFce	4.11×10^{-1}	7.37×10^{-3}	4.26×10^{-1}				
	0.5	HFtoHALL	8.22×10^{-2}	1.52×10^{-3}	8.58×10^{-2}				
	0.5	HFtoLI	$\mathcal{O}(10^{-5})$	$\mathcal{O}(10^{-6})$	$\mathcal{O}(10^{-5})$				
	2.5	HFroof	2.95×10^{-1}	4.87×10^{-3}	3.54×10^{-1}				
HF Gold	0.5	hole22	2.83×10^{-1}	1.65×10^{-2}	3.07×10^{-1}				
	0.5	hole23	2.70×10^{-2}	5.83×10^{-3}	3.34×10^{-2}				
	0.5	HFcl	1.70×10^{-1}	3.21×10^{-3}	1.76×10^{-1}				
	0.5	HFce	4.11×10^{-1}	7.37×10^{-3}	4.26×10^{-1}				
	0.5	HFtoHALL	8.22×10^{-2}	1.52×10^{-3}	8.58×10^{-2}				
	0.5	HFtoLI	$\mathcal{O}(10^{-5})$	$\mathcal{O}(10^{-6})$	$\mathcal{O}(10^{-5})$				
	2.5	HFroof	2.95×10^{-1}	4.87×10^{-3}	3.54×10^{-1}				
HF Gold	0.5	hole22	2.83×10^{-1}	1.65×10^{-2}	3.07×10^{-1}				
	0.5	hole23	2.70×10^{-2}	5.83×10^{-3}	3.34×10^{-2}				
	0.5	HFcl	1.70×10^{-1}	3.21×10^{-3}	1.76×10^{-1}				
	0.5	HFce	4.11×10^{-1}	7.37×10^{-3}	4.26×10^{-1}				
	0.5	HFtoHALL	8.22×10^{-2}	1.52×10^{-3}	8.58×10^{-2}				
	0.5	HFtoLI	$\mathcal{O}(10^{-5})$	$\mathcal{O}(10^{-6})$	$\mathcal{O}(10^{-5})$				
	2.5	HFroof	2.95×10^{-1}	4.87×10^{-3}	3.54×10^{-1}				
HF Gold	0.5	hole22	2.83×10^{-1}	1.65×10^{-2}	3.07×10^{-1}				
	0.5	hole23	2.70×10^{-2}	5.83×10^{-3}	3.34×10^{-2}				
	0.5	HFcl	1.70×10^{-1}	3.21×10^{-3}	1.76×10^{-1}				
	0.5	HFce	4.11×10^{-1}	7.37×10^{-3}	4.26×10^{-1}				
	0.5	HFtoHALL	8.22×10^{-2}	1.52×10^{-3}	8.58×10^{-2}				
	0.5	HFtoLI	$\mathcal{O}(10^{-5})$	$\mathcal{O}(10^{-6})$	$\mathcal{O}(10^{-5})$				
	2.5	HFroof	2.95×10^{-1}	4.87×10^{-3}	3.54×10^{-1}				
HF Gold	0.5	hole22	2.83×10^{-1}	1.65×10^{-2}	3.07×10^{-1}				
	0.5	hole23	2.70×10^{-2}	5.83×10^{-3}	3.34×10^{-2}				
	0.5	HFcl	1.70×10^{-1}	3.21×10^{-3}	1.76×10^{-1}				
	0.5	HFce	4.11×10^{-1}	7.37×10^{-3}	4.26×10^{-1}				
	0.5	HFtoHALL	8.22×10^{-2}	1.52×10^{-3}	8.58×10^{-2}				
	0.5	HFtoLI	$\mathcal{O}(10^{-5})$	$\mathcal{O}(10^{-6})$	$\mathcal{O}(10^{-5})$				
	2.5	HFroof	2.95×10^{-1}	4.87×10^{-3}	3.54×10^{-1}				
HF Gold	0.5	hole22	2.83×10^{-1}	1.65×10^{-2}	3.07×10^{-1}				
	0.5	hole23	2.70×10^{-2}	5.83×10^{-3}	3.34×10^{-2}				
	0.5	HFcl	1.70×10^{-1}	3.21×10^{-3}	1.76×10^{-1}				
	0.5	HFce	4.11×10^{-1}	7.37×10^{-3}	4.26×10^{-1}				
	0.5	HFtoHALL	8.22×10^{-2}	1.52×10^{-3}	8.58×10^{-2}				
	0.5	HFtoLI	$\mathcal{O}(10^{-5})$	$\mathcal{O}(10^{-6})$	$\mathcal{O}(10^{-5})$				
	2.5	HFroof	2.95×10^{-1}	4.87×10^{-3}	3.54×10^{-1}				
HF Gold	0.5	hole22	2.83×10^{-1}	1.65×10^{-2}	3.07×10^{-1}				
	0.5	hole23	2.70×10^{-2}	5.83×10^{-3}	3.34×10^{-2}				
	0.5	HFcl	1.70×10^{-1}	3.21×10^{-3}	1.76×10^{-1}				
	0.5	HFce	4.11×10^{-1}	7.37×10^{-3}	4.26×10^{-1}				
	0.5	HFtoHALL	8.22×10^{-2}	1.52×10^{-3}	8.58×10^{-2}				
	0.5	HFtoLI	$\mathcal{O}(10^{-5})$	$\mathcal{O}(10^{-6})$	$\mathcal{O}(10^{-5})$				
	2.5	HFroof	2.95×10^{-1}	4.87×10^{-3}	3.54×10^{-1}				
HF Gold	0.5	hole22	2.83×10^{-1}	1.65×10^{-2}	3.07×10^{-1}				
	0.5	hole23	2.70×10^{-2}	5.83×10^{-3}	3.34×10^{-2}				
	0.5	HFcl	1.70×10^{-1}	3.21×10^{-3}	1.76×10^{-1}				
	0.5	HFce	4.11×10^{-1}	7.37×10^{-3}	4.26×10^{-1}				
	0.5	HFtoHALL	8.22×10^{-2}	1.52×10^{-3}	8.58×10^{-2}				
	0.5	HFtoLI	$\mathcal{O}(10^{-5})$	$\mathcal{O}(10^{-6})$	$\mathcal{O}(10^{-5})$				
	2.5	HFroof	2.95×10^{-1}	4.87×10^{-3}	3.54×10^{-1}				
HF Gold	0.5	hole22	2.83×10^{-1}	1.65×10^{-2}	3.07×10^{-1}				
	0.5	hole23	2.70×10^{-2}	5.83×10^{-3}	3.34×10^{-2}				
	0.5	HFcl	1.70×10^{-1}	3.21×10^{-3}	1.76×10^{-1}				
	0.5	HFce	4.11×10^{-1}	7.37×10^{-3}	4.26×10^{-1}				
	0.5	HFtoHALL	8.22×10^{-2}	1.52×10^{-3}	8.58×10^{-2}				
	0.5	HFtoLI	$\mathcal{O}(10^{-5})$	$\mathcal{O}(10^{-6})$	$\mathcal{O}(10^{-5})$				
	2.5	HFroof	2.95×10^{-1}	$4.$					

Table 5. Dose rate calculations for LUX, at critical locations indicated in figure 2 and figure 3. The upper half of the table lists results for the 5 GeV monoenergetic electron source, while the lower half holds for the broad spectrum electron source.

	Dose rate limit		Detector position	Dose rate [$\mu\text{Sv h}^{-1}$]				Total
	[$\mu\text{Sv h}^{-1}$]			n	γ	e^-		
LUX 5 GeV	2.5		LUroof	7.64×10^{-1}	1.16×10^{-2}	4.27×10^{-3}		7.95×10^{-1}
	2.5		LUtoLI	1.45×10^{-1}	3.43×10^{-3}	0.00		1.49×10^{-1}
	2.5		LUtoET	8.51×10^{-1}	1.15×10^{-2}	8.43×10^{-3}		9.13×10^{-1}
	2.5		LUdoC	1.36×10^{-1}	9.72×10^{-4}	0.00		1.37×10^{-1}
	2.5		LUtoHF	1.69	2.60×10^{-2}	8.02×10^{-3}		1.82
	2.5		LUtoHALL	7.49×10^{-1}	8.11×10^{-2}	6.08		6.94
	2.5		hole2	7.35×10^{-2}	2.41×10^{-3}	0.00		7.59×10^{-2}
	2.5		hole5	7.45×10^{-2}	1.47×10^{-2}	2.79×10^{-3}		9.19×10^{-2}
	2.5		hole9	6.40×10^{-2}	4.94×10^{-3}	0.00		6.89×10^{-2}
	2.5		hole12	1.14×10^{-1}	1.15×10^{-2}	5.79×10^{-3}		1.31×10^{-1}
LUX Broad	2.5		hole16	3.71×10^{-1}	4.55×10^{-2}	7.73×10^{-3}		4.25×10^{-1}
	2.5		hole19	7.86×10^{-1}	4.64×10^{-2}	5.71×10^{-3}		8.42×10^{-1}
	2.5		LUroof	4.66×10^{-1}	5.60×10^{-3}	9.76×10^{-4}		4.72×10^{-1}
	2.5		LUtoLI	4.20×10^{-2}	1.25×10^{-3}	1.83×10^{-2}		6.51×10^{-2}
	2.5		LUtoET	3.88×10^{-1}	5.95×10^{-3}	0.00		3.94×10^{-1}
	2.5		LUdoC	7.04×10^{-2}	1.05×10^{-3}	3.36×10^{-6}		7.14×10^{-2}
	2.5		LUtoHF	6.29×10^{-1}	1.18×10^{-2}	0.00		6.87×10^{-1}
	2.5		LUtoHALL	5.52×10^{-2}	2.76×10^{-2}	2.31		2.40
	2.5		hole2	8.84×10^{-2}	3.97×10^{-3}	5.46×10^{-4}		9.45×10^{-2}
	2.5		hole5	1.49×10^{-1}	2.92×10^{-3}	2.59×10^{-3}		1.54×10^{-1}
	2.5		hole9	2.36×10^{-2}	4.30×10^{-3}	6.82×10^{-4}		2.86×10^{-2}
	2.5		hole12	8.17×10^{-2}	6.32×10^{-3}	4.51×10^{-3}		9.25×10^{-2}
	2.5		hole16	2.66×10^{-1}	1.72×10^{-2}	6.78×10^{-3}		2.90×10^{-1}
	2.5		hole19	3.05×10^{-1}	2.77×10^{-2}	8.63×10^{-3}		3.44×10^{-1}

Table 6. Dose rate calculations for ETTF, at critical locations indicated in figure 2 and 3. The upper third of the table lists results for the 5 GeV monoenergetic electron source, the middle third for the same source without magnet but lead shielding, while the lower third lists the results for the broad spectrum electron source.

Dose rate limit			Dose rate [$\mu\text{Sv h}^{-1}$]			
	[$\mu\text{Sv h}^{-1}$]	Detector position	n	γ	e^-	Total
ETTF 5 GeV	2.5	ETroof	7.85×10^{-1}	1.28×10^{-2}	3.87×10^{-2}	8.37×10^{-1}
	2.5	ETtoLU	2.46×10^{-1}	4.91×10^{-3}	3.45×10^{-3}	2.63×10^{-1}
	2.5	ETtoSP	7.58×10^{-1}	1.49×10^{-2}	3.21×10^{-3}	7.83×10^{-1}
	2.5	ETdoC	5.35×10^{-2}	5.03×10^{-4}	0.00	5.40×10^{-2}
	2.5	ETtoHALL1	1.10×10^{-1}	7.51×10^{-2}	3.46	3.76
	2.5	ETtoHALL2	6.34×10^{-1}	1.09×10^{-2}	1.29×10^{-2}	6.67×10^{-1}
	2.5	hole4	3.83×10^{-2}	5.30×10^{-3}	5.66×10^{-3}	5.34×10^{-2}
	2.5	hole7	4.83×10^{-2}	4.48×10^{-3}	0.00	5.28×10^{-2}
	2.5	hole11	4.88×10^{-2}	5.78×10^{-3}	0.00	5.46×10^{-2}
	2.5	hole14	1.04×10^{-1}	4.87×10^{-3}	0.00	1.09×10^{-1}
no Magnet	2.5	hole18	8.02×10^{-1}	5.09×10^{-2}	6.50×10^{-3}	8.66×10^{-1}
	2.5	hole21	5.34×10^{-1}	5.42×10^{-2}	8.47×10^{-3}	6.29×10^{-1}
	2.5	ETroof	2.50	8.47×10^{-2}	6.32×10^{-3}	2.61
	2.5	ETtoLU	2.07	4.80×10^{-2}	6.10×10^{-2}	2.20
	2.5	ETtoSP	3.50	8.69×10^{-2}	3.17×10^{-2}	3.84
	2.5	ETdoC	3.96×10^{-3}	8.92×10^{-5}	0.00	4.05×10^{-3}
	2.5	ETtoHALL1	3.95×10^{-1}	5.50×10^{-4}	0.00	4.11×10^{-1}
	2.5	ETtoHALL2	1.69×10^{-2}	1.29×10^{-4}	0.00	1.87×10^{-2}
	2.5	hole4	2.63×10^{-1}	3.84×10^{-2}	0.00	3.02×10^{-1}
	2.5	hole7	4.39×10^{-1}	3.49×10^{-2}	8.98×10^{-2}	5.64×10^{-1}
	2.5	hole11	2.57×10^{-1}	3.34×10^{-2}	1.19×10^{-3}	2.91×10^{-1}
	2.5	hole14	3.62×10^{-1}	4.21×10^{-2}	1.71×10^{-2}	4.22×10^{-1}
	2.5	hole18	4.77	3.42×10^{-1}	2.12×10^{-1}	5.33
	2.5	hole21	5.86	3.93×10^{-1}	5.43×10^{-1}	6.83

Table 6. continued.

	Dose rate limit [$\mu\text{Sv h}^{-1}$]	Detector position	Dose rate [$\mu\text{Sv h}^{-1}$]			
			n	γ	e^-	Total
ETTF	2.5	ETroof	6.86×10^{-1}	9.94×10^{-3}	8.19×10^{-4}	7.00×10^{-1}
Broad	2.5	ETtoLU	2.20×10^{-1}	3.80×10^{-3}	2.86×10^{-3}	2.28×10^{-1}
	2.5	ETtoSP	4.63×10^{-1}	1.03×10^{-2}	2.02×10^{-3}	4.86×10^{-1}
	2.5	ETdoC	2.92×10^{-2}	3.16×10^{-4}	0.00	2.95×10^{-2}
	2.5	ETtoHALL1	3.52×10^{-2}	5.01×10^{-2}	8.84×10^{-1}	1.04
	2.5	ETtoHALL2	2.27×10^{-1}	3.81×10^{-3}	2.83×10^{-3}	2.35×10^{-1}
	2.5	hole4	4.51×10^{-2}	4.40×10^{-3}	4.68×10^{-3}	6.38×10^{-2}
	2.5	hole7	3.92×10^{-2}	8.15×10^{-3}	7.16×10^{-4}	4.80×10^{-2}
	2.5	hole11	6.41×10^{-2}	8.23×10^{-3}	1.04×10^{-3}	7.34×10^{-2}
	2.5	hole14	4.93×10^{-2}	5.30×10^{-3}	7.62×10^{-4}	5.53×10^{-2}
	2.5	hole18	7.01×10^{-1}	8.60×10^{-2}	2.35×10^{-2}	8.19×10^{-1}
	2.5	hole21	9.86×10^{-1}	7.78×10^{-2}	3.98×10^{-2}	1.11

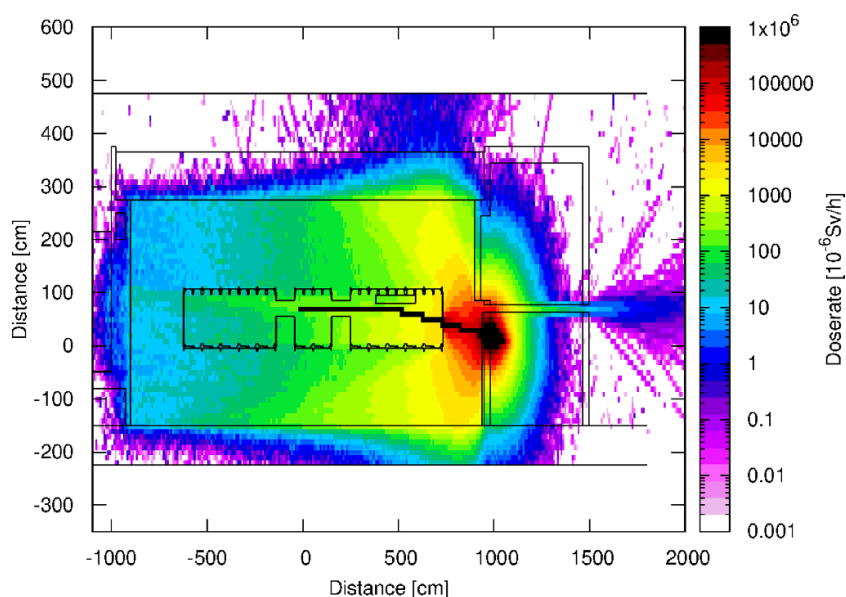


Figure 5. Dose rate in ETTF shown on a vertical plane, for a 5 GeV monoenergetic electron source intersected by a spectrometer magnet.

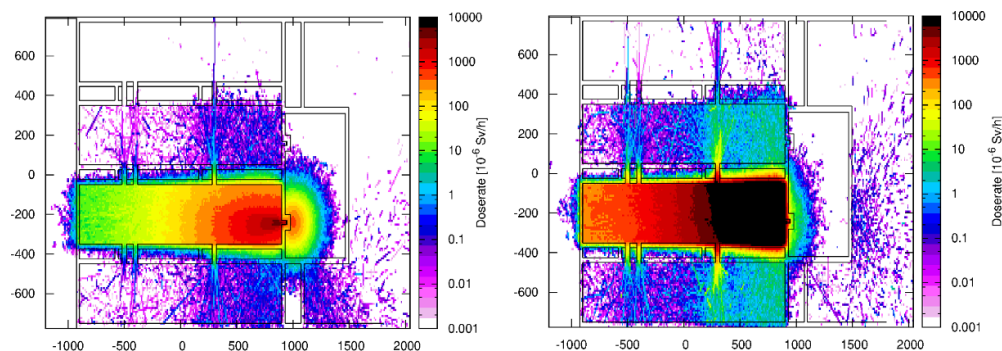


Figure 6. Dose rate distributions for the ETTF cave at the beam line level for 5 GeV monoenergetic electron source. (*Left*) normal setup with spectrometer magnet, (*right*) without spectrometer magnet. In the latter 50 cm lead were employed at both ends of the beam dump channel as shielding.

magnet in place and a 5 GeV monoenergetic electron source with and without the spectrometer magnet.

Since the primary source is the same as in LUX and consisting of highly penetrating electrons, the total dose rate is again reported alongside with the individual contributions from neutrons, gammas and electrons.

For the broad spectrum source, the dose rates in all scoring locations remained below the $2.5 \mu\text{Sv h}^{-1}$ design limit. Out-of-cave doses from neutrons were in general found to be one order of magnitude higher than photon doses and two orders lower compared to electrons.

The lower energy electrons from the broad spectrum source bent downwards, at large angles after travelling in the spectrometer magnet, caused the highest total dose rate of $1.11 \mu\text{Sv h}^{-1}$

to occur behind the nearest laser penetration hole (hole21), inside LUX. Similar to LUX, electrons are scattered through the 5.85 m central beam dump channel (ETtoHALL1) and gave rise to a calculated dose rate of $1.04 \mu\text{Sv h}^{-1}$.

For the 5 GeV monoenergetic source scenario with the spectrometer magnet, the highest dose rate of $3.76 \mu\text{Sv h}^{-1}$ was calculated to occur behind the central beam dump hole (ETtoHALL1), as depicted in figure 5. That was higher than the design limit of $2.5 \mu\text{Sv h}^{-1}$, but less than the maximum allowed local dose rate value of $7.5 \mu\text{Sv h}^{-1}$.

For that particular source and experimental cave, the highest simulated dose rate for CALA of 1.6 kSv/h was recorded inside the central beam dump. In this inaccessible location, the particle fluence locally was calculated to be up to 1.6×10^{10} particles / cm^2 .

The monoenergetic 5 GeV beam without the spectrometer magnet presented a challenging scenario for radiation protection. This is highlighted in figure 6, where the dose rate at beam line level is shown for the case with (left) and without (right) spectrometer magnet.

The employed 50 cm lead bricks at both ends of the central beam dump channel were able to hinder direct electron penetration through the channel. The highest dose rates in the scenario were $2.61 \mu\text{Sv h}^{-1}$ on the roof of the building (ETroof), $3.84 \mu\text{Sv h}^{-1}$ in the SPECTRE cave (ETtoSP), $5.33 \mu\text{Sv h}^{-1}$ and $6.83 \mu\text{Sv h}^{-1}$ in the two of the eastern laser penetration holes (hole18 and hole21) to LUX and SPECTRE respectively.

Although the aforementioned dose rates exceeded the design limit of $2.5 \mu\text{Sv h}^{-1}$, they were below maximum local dose limit of $7.5 \mu\text{Sv h}^{-1}$.

3.5. SPECTRE

For the SPECTRE cave three source types were simulated (for details see table 2): a 500 MeV electron source at a repetition rate of 1 Hz. A broad spectrum electron source with energies up to 500 MeV, also generated with 1 Hz repetition frequency. Finally, 70 MeV monoenergetic electrons with 1 kHz repetition frequency.

Table 7 summarises the dose rates outside the cave in all scoring locations for the three source configurations. Except for one case, the calculated dose rates were at least one order of magnitude below the respective limits, either that of $2.5 \mu\text{Sv h}^{-1}$ for supervised areas or that of $0.5 \mu\text{Sv h}^{-1}$ for unclassified areas.

The sole exception to this was in the critical location behind one of the laser penetration holes leading to ETTF (hole20), for the 70 MeV monoenergetic electrons with 1 kHz repetition frequency. There the dose rate was quantified to exceed the $2.5 \mu\text{Sv h}^{-1}$ design limit ($3.62 \mu\text{Sv h}^{-1}$), but still below the maximum allowed local dose rate of $7.5 \mu\text{Sv h}^{-1}$.

Neutrons dominated again the out-of-cave doses.

4. Discussion

As presented in section 3 and detailed in table 3 - table 7, by employing adequate beam dumps matched to beam-divergence, magnets, passive shielding and laser pulse repetition limits, the simulated dose rates remained mostly below the design limits of the CALA facility ($0.5 \mu\text{Sv h}^{-1}$ for unclassified and $2.5 \mu\text{Sv h}^{-1}$ for supervised areas).

The highest dose areas in each cave were directly correlated to the location of the respective beam dump. For the LUX, ETTF and SPECTRE caves, the beam was terminated in the central beam dump, at the eastern end of each cave. This meant that the dose was higher in that part of these caves and in the experimental hall behind it. LION and HF contain individual beam dumps, approximately located at the center of these caves. Therefore, the high dose areas in

Table 7. Dose rate calculations for SPECTRE, at critical locations indicated in figure 2 and 3. The upper third of the table lists results for the 70 MeV monoenergetic electron source at 1 kHz, the middle third for the 500 MeV monoenergetic electron source at 1 Hz, while the lower third represents the broad spectrum electron source at 1 Hz.

	Dose rate limit		Dose rate [$\mu\text{Sv h}^{-1}$]			
	[$\mu\text{Sv h}^{-1}$]	Detector position	n	γ	e^-	Total
SPECTRE 70 MeV	2.5	SProof	5.07×10^{-3}	2.33×10^{-3}	0.00	7.40×10^{-3}
	2.5	SProET	6.92×10^{-4}	8.54×10^{-4}	0.00	1.55×10^{-3}
	2.5	SPdoC	0.00	1.47×10^{-4}	0.00	1.47×10^{-4}
	2.5	SProHALL1	0.00	0.00	0.00	0.00
	2.5	SProHALL2	0.00	0.00	0.00	0.00
	2.5	SProHALL3	0.00	0.00	0.00	0.00
	0.5	SProLAB	0.00	0.00	0.00	0.00
	2.5	hole6	2.03×10^{-2}	9.05×10^{-3}	0.00	2.94×10^{-2}
	2.5	hole13	1.54×10^{-2}	1.05×10^{-2}	0.00	2.59×10^{-2}
	2.5	hole20	1.30	1.39	9.25×10^{-1}	3.62
SPECTRE 500 MeV	2.5	SProof	4.82×10^{-2}	8.19×10^{-4}	1.15×10^{-4}	4.91×10^{-2}
	2.5	SProET	6.29×10^{-2}	1.34×10^{-3}	6.55×10^{-4}	6.67×10^{-2}
	2.5	SPdoC	5.89×10^{-3}	9.22×10^{-5}	0.00	5.98×10^{-3}
	2.5	SProHALL1	5.15×10^{-2}	1.42×10^{-3}	1.90×10^{-3}	5.48×10^{-2}
	2.5	SProHALL2	5.09×10^{-2}	6.96×10^{-4}	0.00	5.16×10^{-2}
	2.5	SProHALL3	1.63×10^{-2}	2.02×10^{-4}	0.00	1.65×10^{-2}
	0.5	SProLAB	3.20×10^{-2}	6.03×10^{-4}	1.79×10^{-4}	3.28×10^{-2}
	2.5	hole6	1.53×10^{-2}	1.54×10^{-3}	4.12×10^{-4}	1.73×10^{-2}
	2.5	hole13	1.62×10^{-2}	1.91×10^{-3}	5.66×10^{-4}	1.87×10^{-2}
	2.5	hole20	1.43×10^{-1}	2.05×10^{-2}	1.06×10^{-2}	1.79×10^{-1}

Table 7. continued.

	Dose rate limit [$\mu\text{Sv h}^{-1}$]	Detector position	Dose rate [$\mu\text{Sv h}^{-1}$]			
			n	γ	e^-	Total
SPECTRE Broad	2.5	SProof	3.21×10^{-2}	5.85×10^{-4}	0.00	3.27×10^{-2}
	2.5	SProET	3.05×10^{-2}	6.61×10^{-4}	0.00	3.12×10^{-2}
	2.5	SProC	1.69×10^{-3}	9.00×10^{-5}	0.00	1.78×10^{-3}
	2.5	SProHALL1	1.47×10^{-2}	9.63×10^{-4}	0.00	1.56×10^{-2}
	2.5	SProHALL2	1.43×10^{-2}	1.07×10^{-3}	0.00	1.54×10^{-2}
	2.5	SProHALL3	6.87×10^{-3}	8.69×10^{-5}	2.74×10^{-4}	7.23×10^{-3}
	0.5	SProLAB	1.29×10^{-2}	2.52×10^{-4}	0.00	1.34×10^{-2}
	2.5	hole6	9.22×10^{-3}	1.71×10^{-3}	7.53×10^{-4}	1.17×10^{-2}
	2.5	hole13	1.62×10^{-2}	2.16×10^{-3}	3.05×10^{-3}	2.14×10^{-2}
	2.5	hole20	2.01×10^{-1}	1.51×10^{-1}	3.77×10^{-1}	8.33×10^{-1}

these caves were estimated to be in their middle, which in its turn resulted in the highest dose rates outside these caves to occur behind the walls in the direct vicinity of the beam dumps.

Common to all caves, as expected, was the trend for high dose rates to be present behind the laser penetration holes that are near beam dumps. The locations behind the holes, however, are below the false floor, hence not readily accessible.

Secondary neutrons were in the majority of the cases the dominant contribution to dose rates calculated outside a cave in operation. The initial beam and charged secondaries were usually fully contained in the beam dumps, but secondary neutrons created in these volumes with highly directional fluences, gave rise to considerable doses outside the caves. A different situation was observed when beams were hitting the central beam dump and the x-ray extraction channels were open (LUX, ETTF, SPECTRE caves). In these cases, high energy electrons not adequately bent by the spectrometer magnets were the main component of the calculated out-of-cave high dose rate. The leakage of electrons through the x-ray extraction channels can be further increased due to scattering in the chamber walls intersecting the beam. Thicker walls significantly increase the angular distribution of the electron beam, allowing a larger part of it to go through the beam dump channels.

The high energy electrons produced in ETTF and SPECTRE yield a non-negligible fluence of muons (up to about 1000 muons/cm²), approximately two orders of magnitude lower than the maximum neutron fluence. These muons are predominantly produced at shallow locations of the central beam dump. They display a broad energy spectrum with energies reaching up to a few GeV. Muons with such energies have a maximum range in water of 3–4 m, which means that they cannot escape the central 5.85 m thick concrete beam dump. Therefore, their contribution to the dose rate outside the caves is negligible.

The maximum quantified dose rate outside a cave in operation was 6.94 $\mu\text{Sv h}^{-1}$ and was estimated for a monoenergetic 5 GeV electron source, behind the central beam dump of LUX (LUtoHALL). That location is one of the critical points of the CALA design. Despite the massive central beam dump, two channels through it are required in order to allow for the transport of x-ray beams from the experimental caves LUX and ETTF to the experimental hall to the east. Behind these two channels dose rates were expected to be high. The almost 3-fold excess of the 2.5 $\mu\text{Sv h}^{-1}$ design limit for supervised areas was mainly attributed to high energy electrons escaping through one of the central beam dump channels. The dose was below the maximum locally allowed dose rate of 7.5 $\mu\text{Sv h}^{-1}$, which means that this particular location can be made temporarily inaccessible.

A similar dose rate (6.83 $\mu\text{Sv h}^{-1}$) was calculated to leak through one of the laser penetration holes towards SPECTRE (hole21), in the case of the most demanding configuration in ETTF, that of a monoenergetic 5 GeV electron source without a spectrometer magnet. Due to the lack of magnetic deflection, almost the entire electron beam hit a small area of the central beam dump (the lead blocking the beam dump channel) and created a high radiation environment in a small section of the ETTF cave. The creation of secondary neutrons there was the primary dose rate component leaking through the laser penetration hole most proximal to the beam dump. As in the previous case, this dose rate was also below the maximum locally allowed rate of 7.5 $\mu\text{Sv h}^{-1}$.

Excess of the dose rate limit for unclassified areas (0.5 $\mu\text{Sv h}^{-1}$ limit) was estimated for a few occasions concerning the LION and HF caves simulated operation. For LION the highest dose rate (1.06 $\mu\text{Sv h}^{-1}$) occurred at the north corridor (LIc) in the ¹²C source case and was mainly attributed to the directional neutron fluence escaping the hybrid beam dump. For HF, the respective excess dose rate of 1.06 $\mu\text{Sv h}^{-1}$ was calculated behind one of the laser penetration holes (hole22) for the proton source case. Again the main component of the dose rate originated from secondary neutrons, backscattered from the concrete beam dump. The fact that

for HF, contrary to LION, it was the proton rather than the ^{12}C source the most demanding scenario in terms of radiation protection was due to the fact that the maximum ^{12}C ion energy in HF was assumed to be half of that in LION (for details see table 2).

Due to the ^{12}C -ion energy spectrum in LION, elevated dose rates, mostly stemming from secondary neutrons were calculated. This necessitated the design of an optimised beam dump for that cave. A full concrete beam dump of the same volume would stop the beam before penetrating deep enough and most of the produced secondaries would back-scatter (see figure 4 - *top*). A full water beam dump would stop the beam deeper in the beam dump, but the lower density and stopping power of water compared to concrete would still allow a large fraction of the generated secondaries to escape, especially towards the forward direction (see figure 4 - *middle*). The hybrid beam dump stops the beam approximately in the middle of its volume, containing more efficiently the secondaries by enclosing them in a water cavity surrounded by concrete (see figure 4 - *bottom*).

One of the main goals of the CALA radiation protection design was to allow caves and experimental areas neighbouring a cave, in which the laser is in operation, to remain accessible. This goal was in general achieved in our simulation study, with a few exceptions at a handful of locations (dose rates $> 2.5 \mu\text{Sv h}^{-1}$): in the experimental hall, when LUX or ETTF (only for 5 GeV monoenergetic) were in operation, due to the electron leakage through the central beam dump channels. In SPECTRE and LUX when ETTF was in operation with 5 GeV monoenergetic electrons without spectrometer magnet due to neutron dose. In ETTF when SPECTRE was in operation with 70 MeV at the high repetition rate of 1 kHz, again due to neutrons.

In this study we have calculated the dose rate from each individual cave being in operation, without assuming cumulative effects due to operation of multiple caves in parallel. Four out of the five CALA caves (LION, HF, LUX and ETTF) are seeded by the ATLAS-3000 laser and will not be operated simultaneously. ETTF and SPECTRE (seeded by the PSF-pro laser) can in principle be operated at the same time, which means that their cumulative dose rate should be taken into account. A critical location which would be accessible during a simultaneous operation of ETTF and SPECTRE is the vicinity of ETtoHALL2 and SPtoHALL1. This is the area with the highest overlap of dose leakage originated by ETTF and SPECTRE. At this location, the cumulative dose rate for the worst case scenario sources (ETTF 5 GeV monoenergetic, SPECTRE 500 MeV monoenergetic) would be $7.22 \times 10^{-1} \mu\text{Sv h}^{-1}$ ($6.67 \times 10^{-1} \mu\text{Sv h}^{-1} + 5.48 \times 10^{-2} \mu\text{Sv h}^{-1}$), which is much lower than the required dose rate limit.

Additional, beyond the nominal, material and equipment intersecting the electron beam might significantly change the source characteristics. This in its turn can have a large impact on the dose rate outside the caves. An extreme example of such a scenario is the 5 GeV ETTF electron beam passing through the thick 2.5 cm vacuum chamber walls instead of the 3 mm extraction window. This was estimated to increase the dose rate in the critical location ETtoHALL1 by up to a factor of 10. Therefore, constant monitoring of the dose rate at multiple locations outside the caves is envisaged.

There are a few factors that justify the design choice of the facility without a maze at the entrance to each cavern, maximising cavern space. The first is the fact that the use of thick concrete doors mitigates the need for a maze (in most radiation treatment facilities, the maze makes up for the shielding required due to the use of glass and thin metal doors). In addition, for all experimental caverns except for HF, the entrance is located at 180° with respect to the laser propagation direction towards the target. This is the direction with the lowest particle fluence, thus resulting to a low dose rate. Furthermore, the source parameters used in this MC study and yielding in some cases dose rates near the allowed limits, are rather optimistic (worst

case scenario for shielding). Especially for biomedical applications, higher energies/fluences are not necessary.

Finally, in the unlikely case that the laser and targetry enable us to reach higher energies/fluences in the far future of CALA, decreasing the repetition rate for some particular experiments/sources would allow us to remain within the radiation protection limits.

5. Conclusion

Monte Carlo simulations were used to design and validate the radiation protection setup of the multi-purpose laser-particle acceleration facility CALA. Our study showed that dose from secondary neutrons was the major contribution in dose rates calculated outside experimental caves in operation. In addition to that, any holes or extraction channels would allow parts of the beam to escape the caves, also resulting in high dose rates. The presented design achieved the goal of dose rates below $7.5 \mu\text{Sv h}^{-1}$ outside any cave in operation. The present trial operation of CALA is used to assure that the provisions concerning the dose limits are met.

Acknowledgment

The work presented in this documents was supported by the German research foundation (DFG) Cluster of Excellence Munich Centre for Advanced Photonics (EXC 158). We acknowledge the work performed by TÜV SÜD Nuclear Technologies, Warrington, UK as the starting point for our studies and Florian Saran and Klaus Wirgler for help with the preparation of technical drawings.

ORCID iDs

Franz S Englbrecht  <https://orcid.org/0000-0003-2613-9783>

Florian H Lindner  <https://orcid.org/0000-0003-4279-1747>

References

- [1] Tajima T and Dawson J M 1979 Laser Electron Accelerator *Phys. Rev. Lett.* **43** 268
- [2] Strickland D and Mourou G 1985 Compression of Amplified Chirped Optical Pulses *Opt. Commun.* **56** 219
- [3] Linz U and Alonso J 2016 Laser-driven ion accelerators for tumor therapy revisited *Phys. Rev. Accel. Beams* **19** 124802–10
- [4] Schreiber J, Bolton P and Parodi K 2016 Invited Review Article: “Hands-on” laser-driven ion acceleration: A primer for laser-driven source development and potential applications *Rev. Sci. Instrum.* **87** 071101
- [5] Esarey E, Schroeder C B and Leemans W P 2009 Physics of laser-driven plasma-based electron accelerators *Rev. Mod. Phys.* **81** 1229–85
- [6] Richter C et al 2016 First clinical application of a prompt gamma based in vivo proton range verification system *Radiother. Oncol.* **118** 232–7
- [7] van de Water S, Safai S, Schippers J M, Weber D C and Lomax A J 2019 Towards FLASH proton therapy: the impact of treatment planning and machine characteristics on achievable dose rates *Acta Oncol.* **58** 1463–9
- [8] Wenz J, Schleede S, Khrennikov K, Bech M, Thibault P, Heigoldt M, Pfeiffer F and Karsch S 2016 Quantitative X-ray phase-contrast microtomography from a compact laser-driven betatron source *Nat. Commun.* **6** 7568
- [9] Wenz J et al 2019 Dual-energy electron beams from a compact laser-driven accelerator *Nat. Photonics* **13** 263–9

- [10] Gonsalves A J *et al* 2015 Generation and pointing stabilization of multi-GeV electron beams from a laser plasma accelerator driven in a pre-formed plasma waveguide *Phys. Plasmas* **22** 056703–8
- [11] Lu W, Tzoufras M, Joshi C, Tsung F S, Mori W B, Vieira J, Fonseca R A and Silva L O 2007 Generating multi-GeV electron bunches using single stage laser wakefield acceleration in a 3D nonlinear regime *Phys. Rev. ST Accel. Beams* **10** 061301
- [12] Bundesministerium für Umwelt, Naturschutz und nukleare Sicherheit 2018 Verordnung zum Schutz vor der schädlichen Wirkung ionisierender Strahlung (Strahlenschutzverordnung - StrlSchV) *Bundesgesetzblatt BGBl.* **41** 2034
- [13] Borne F, Delacroix D, Gelé J M, Massé D and Amiranoff F 2012 Radiation protection for an ultra-high intensity laser *Radiat. Prot. Dosim.* **102** 61–70
- [14] Ankerhold U, Hupe O and Ambrosi P 2009 Deficiencies of active electronic radiation protection dosimeters in pulsed fields *Radiat. Prot. Dosim.* **135** 149–53
- [15] Ambrosi P, Borowski M and Iwatschenko M 2010 Considerations concerning the use of counting active personal dosimeters in pulsed fields of ionising radiation *Radiat. Prot. Dosim.* **139** 483–93
- [16] Gao Y *et al* 2017 An automated, 0.5 Hz nano-foil target positioning system for intense laser plasma experiments *High Power Laser Sci* **5** 12
- [17] Daido H, Nishiuchi M and Pirozhkov A S 2012 Review of laser-driven ion sources and their applications *Rep. Prog. Phys.* **75** 056401–72
- [18] Macchi A, Borghesi M and Passoni M 2012 Ion acceleration by superintense laser-plasma interaction *Rev. Mod. Phys.* **85** 751–93
- [19] Lindner F H *et al* 2018 A novel approach to electron data background treatment in an online wide-angle spectrometer for laser-accelerated ion and electron bunches *Rev. Sci. Instrum.* **89** 013301
- [20] Lindner F H *et al* 2017 Towards swift ion bunch acceleration by high-power laser pulses at the Centre for Advanced Laser Applications (CALA) *Nucl. Instrum. Methods Phys. Res. B: Beam Interactions with Materials and Atoms* **402** 354–7
- [21] Habs D, Thierolf P G, Gross M, Allinger K, Bin J, Henig A, Kiefer D, Ma W and Schreiber J 2011 Introducing the fission-fusion reaction process: using a laser-accelerated Th beam to produce neutron-rich nuclei towards the N=126 waiting point of the r-process *Appl. Phys. B* **103** 471–84
- [22] Forster Ingenieurgesellschaft (www.forster-bau.de/referenzen.html), (www.forster-bau.de/sandwich-construction.html) (Accessed 1 July 2020)
- [23] Snavely R A *et al* 2000 Intense high-energy proton beams from petawatt-laser irradiation of solids *Phys. Rev. Lett.* **85** 2945–8
- [24] Ferrari A, Sala P R, Fasso A and Ranft J 2012 FLUKA: a multi-particle transport code *CERN-2005-10, INFN/TC_05/11, SLAC-R-773*
- [25] Böhlen T T *et al* 2014 The FLUKA Code: Developments and challenges for high energy and medical applications *Nucl. Data Sheets* **120** 211–14
- [26] Döpp A, Hehn L, Götzfried J, Wenz J, Gilljohann M, Ding H, Schindler S, Pfeiffer F and Karsch S 2018 Quick x-ray microtomography using a laser-driven betatron source *Optica* **5** 056703–8
- [27] Gaillard S A *et al* 2011 Increased laser-accelerated proton energies via direct laser-light-pressure acceleration of electrons in microcone targets *Phys. Plasmas* **18** 056710